GREEN-LASER ADDITIVE MANUFACTURE OF A GRCOP-42 LOX/LCH4 COMBUSTION CHAMBER WITH COMPLIANT FIREWALL

GLASGOW / 20-23 MAY 2024

Iain Waugh[1,4], Elliott Brookes-Gayton[1], Matt Coates[1], James Macfarlane[1], Daniel Heußen[2], and Chris Dalton[3]

[1] *Airborne Engineering Ltd., Westcott Venture Park, Aylesbury, UK*
[2] *Fraunhofer ILT, Aachen, Germany*
[3] *Manufacturing Technology Centre, Coventry, UK*
[4] *Corresponding author: iain@ael.co.uk*

KEYWORDS:

Additive manufacture, green laser, GRCop-42, combustion chamber, compliant firewall

ABSTRACT

Additive manufacture of copper alloys has typically used powder bed fusion (PBF) machines fitted with red (1060-1080nm) lasers. However, copper is very reflective at these frequencies - less than 30% of the energy is absorbed - and therefore high power lasers are required. Using green (515nm) lasers offers energy absorption up to 60%, which will result in better part integrity and faster manufacturing times.

Green-laser processes were optimised for GRCop-42 using small coupons and parameter sweeps of laser power, hatch distance, scanning speed and beam compensation. Excellent bulk densities of up to 99.99% were obtained, which may reduce the necessity for the additional hot-isostatic pressing post-processing step that is often used for liquid rocket engine combustion chambers.

A 20kN demonstrator combustion chamber was designed, using dual LOX/LCH4 cooling and GRCop-42 slip liners inside an IN718 structural jacket. The slip liners have expansion slots in between coolant channels in order to provide compliance at the firewall, with the intention of reducing the magnitude of stress cycling and therefore increasing the fatigue life of the firewall. Samples of these expansion slots were tested to ascertain their compressive and tensile performance. Using these expansion slots to supply transpiration cooling was also demonstrated.

1. INTRODUCTION

Liquid rocket engine (LRE) combustion chambers must endure extremes of temperature, heat flux and pressure. This heat flux occurs on the inside of the combustion chamber, and is only endured by transferring the heat to a coolant (usually a propellant) running through coolant channels behind a thin firewall. A LRE combustion chamber design must account for firewall stresses generated by several mechanisms: thermal stress, pressure stress and thermal expansion mismatch to structural jackets. In areas of high heat flux, such as the throat, the thermal stresses in the firewall typically dominate and this area is usually the key limitation in chamber design and lifetime. For a given heat flux, the thermal stress is inversely proportional to the thermal conductivity, meaning that that maximising thermal conductivity is key for high performance combustion chambers.

Copper alloys have been used extensively for high performance LRE combustion chambers due to their combination of high thermal conductivity and strength at high temperatures, which is ideal for resisting thermal stresses. For LRE applications the material properties of the alloy at elevated temperature are extremely important for determining the maximum engine performance and lifetime. The key properties include strength, thermal conductivity, low-cycle fatigue (LCF) and creep performance. During hot-firing a LRE firewall undergoes cyclic loading due to thermal and pressure stress during start-up and shutdown, and thermal stress during operation. For a cryogenic engine, during start-up a copper liner chills down faster than the structural jacket causing a tensile stress in the firewall alongside the pressure stress. After ignition the firewall heats rapidly, whereas the jacket does not, causing a compressive stress in the firewall [1] . At engine shutdown, the firewall cools quickly again leading to a tensile stress. The tensile and compressive strain can be of order 1 or 2% [1]. Combustion chambers therefore typically fail from a combination of low-cycle fatigue (LCF) and cyclic plastic strain accumulation (ratchetting) for each start-up and shutdown, and high temperature creep from steady-state operation, resulting in a 'dog-house' failure mode at the firewall [23].

AM has the potential to enhance the design freedom of combustion chambers, whilst greatly reducing the time and complexity of the build process for a combustion chamber. When compared to a traditional electroforming route, the forging, bulk shape machining, channel machining, wax filling of channels, conductivising (e.g. silver powder burnished into the wax) and electroforming closeout can all be replaced with a single print operation. In the literature combustion chambers have been successfully demonstrated from copper alloys such as GRCop-42/84 [11, 10] and CuCrZr [7, 8, 9, 12, 13].

Additive manufacture of copper alloys has typically used powder bed fusion (PBF) machines fitted with red (1060-1080nm) lasers. High laser power is required to maintain a melt pool because copper has a very high thermal conductivity and therefore heat is quickly lost to the surrounding material. Furthermore, copper is very reflective at red laser frequencies; less than 30% of the laser energy is absorbed. This leads to narrow process windows and melt pool instabilities [3]. Modification of the powder can lead to increased absorption of around 60% or more, for example by surface oxidation [4], nickel coating [5] or adding additional materials such as carbon to the bulk material [5]. However, the addition of coatings or dopants will alter the alloy composition and will therefore have some affect on the resulting material properties.

An alternative way to increase absorption without changing the alloy composition is to use green lasers. Green (515nm) lasers offer energy absorption up to 60%, which therefore gives the potential for better part quality (higher density and fewer defects) and faster manufacturing times than traditional red laser systems [2]. However, the beam spot size of green lasers is limited by the beam quality of current disc lasers and is around double the size of equivalent power red lasers. This could have a negative impact on the resolution of small features, such as thin walls or small diameter holes.

2. THE CUFAM PROJECT

The Copper for Additive Manufacture (CufAM) project is an ongoing collaboration between The Manufacturing Technology Centre (MTC), Airborne Engineering (AEL), both based in the UK, and the Fraunhofer-Institut für Lasertechnik (ILT), based in Aachen, Germany. Under ESA GSTP funding this collaboration aimed to investigate the potential benefits of using green-laser additive manufacture for liquid rocket engine combustion chambers.

PBF machines fitted with green lasers have only recently been available on the open market, often with limited laser power and build volume. The CufAM project uses a custom developed machine housed at Fraunhofer ILT, Aachen, with an Aconity Midi build chamber of diameter 170mm and height 200mm, and a Trumpf Trudisk 1020 laser beam (1000W).

GRCop-42 is a Cu-Cr-Nb alloy that is designed for use in LRE applications. It is dispersion hardened by Cr_2Nb precipitates, which are stable until beyond the melting point of copper, and therefore the alloy maintains strength to very high temperatures. The large volume of fine, hard precipitates also leads to good LCF and creep performance [14]. Both Cr and Nb have minimal solubilities in copper, limiting the decrease in thermal conductivity [14].

This paper describes first describes the laser parameter optimisation undertaken to obtain the best properties for GRCop-42 using green lasers. This paper then describes the design of a LRE combustion chamber demonstrator and the geometry samples manufactured from GRCop-42, in particular those with a novel geometry designed to reduce cyclic firewall stresses. The paper concludes with an outlook on the future work expected in the CufAM project.

3. GRCOP-42 POWDER ANALYSIS

There are several suppliers of GRCop-42 powder; Carpenter Additive was used for this project. Powder was checked and analysed before beginning further work. Figure 1 shows the powder size distribution of the received GRCop-42 powder, and Table 1 shows the chemical composition results. Most of the composition was within specification, with the exception of the Niobium which was slightly lower than the optimum range for maintaining the Cr/Nb balance that governs the dispersion hardening of the alloy, but a slight excess of Cr does suppress detrimental Nb formation [6].

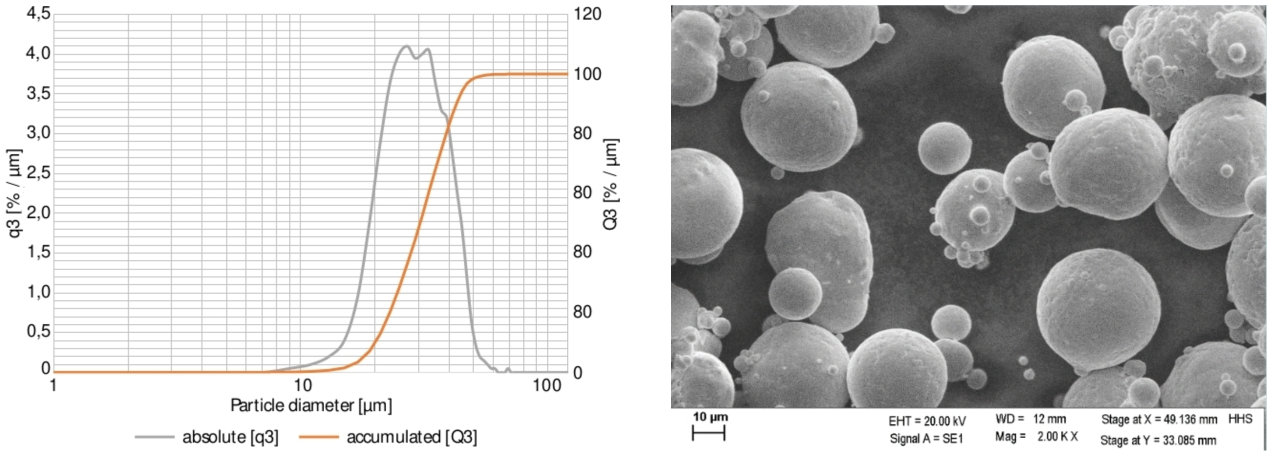

(a) Powder size distribution

(b) SEM micrograph

Figure 1: Analysis of the GRCop-42 powder size distribution and shape.

	Specification	Measured
Cr	3.1-3.4%	3.2%
Nb	2.7-3.0%	2.5%
Si	0.035%	0.088%
O	0.04%	0.032%
Al	0.06%	0.010%
Fe	0.025%	0.007%
N		< 0.010%
H		0.0014%

Table 1: Chemical analysis of the alloying elements and contaminants in the received GRCop-42 powder.

4. GREEN-LASER PARAMETER TUNING

Developing a PBF process requires a multi-step procedure to determine the processing window where good part quality is achieved. First, bulk laser parameters are investigated in order to obtain good part density. The key bulk laser parameters are laser power (P_L), scanning speed (v_{SCAN}) and hatch distance (Δy_S). Second, contour parameters are investigated to determine optimum conditions for the part surfaces. Attention must be placed on not just the porosity of the contour region itself, but also the consolidation between the hatch and contour regions, the resulting surface finish, and the impact on surfaces of all orientations. This phase can also be used to understand the impact of scaling factors and beam compensation on built parts.

4.1. Bulk density

Bulk laser parameters were varied in an equally-distanced partial factorial test plan. Laser power was varied from 430 W to 940 W in six steps; scanning speed from 400 mm/s to 2000 mm/s in six steps; and hatch distance from 150 µm to 400 µm in 8 steps. Step resolution for the lower hatch distance values was 25 µm, and for the upper values was 50 µm. Layer thickness was fixed to 60 µm, chosen because it was expected to give an acceptable trade-off between surface quality in overhangs, and productivity for larger components. With the combustion chamber considered a large part, occupying a significant portion of the build volume, this trade-off was deemed appropriate. The laser beam diameter was also fixed at 250 µm, due to the machine configuration for the desired size of the build volume (diameter 150 mm). Process development via density analysis was typically conducted on cube specimens of side 10mm.

Two phases of testing were undertaken. First, a screening phase where a wider set of parameters was investigated in order to downselect the best parameter combinations. Second, a validation and further testing phase to understand the reproducibility of initial results. Due to the high sensitivity of the testing procedure to the influence of single processing parameters, vectors were aligned parallel to cube edges, with a vector length of 10 mm to fit within the parts. In the first trials, no contouring was applied. The vector scanning pattern was rotated every layer by 90°, and scanning order was always oriented against the shielding gas flow.

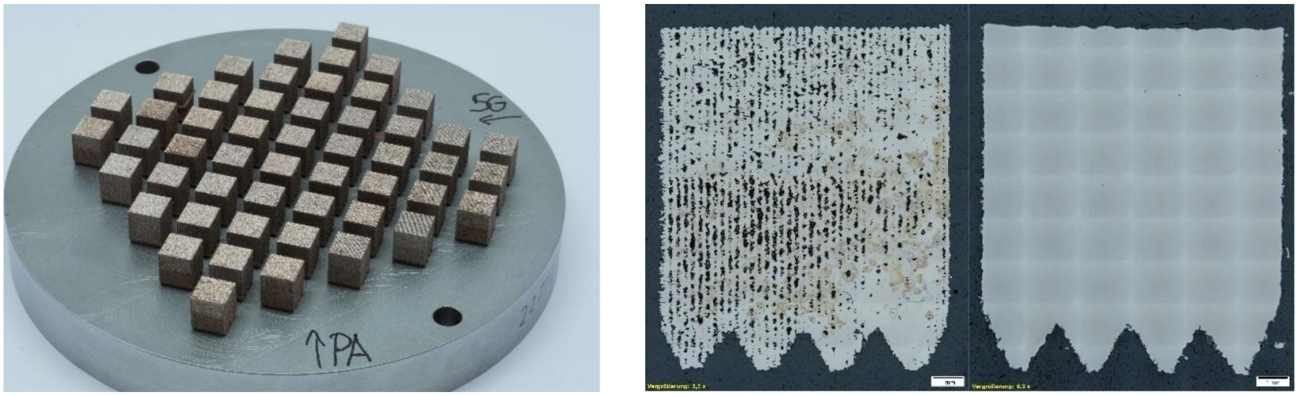

(a) Density samples *(b) Comparison of lowest and highest density achieved*

Figure 2: Density samples produced and comparison of the worst and best results.

Figure 2 shows the initial build samples and micrographs of the lowest and highest density samples. Hatch distances above 200µm and laser powers below 644W were eliminated from further testing. Figure 3 shows the results from validation testing in the phase 2, where each result is the median from up to six specimens. Reproducible part densities of over 99.9% were achieved. Such excellent densities are significant because they may remove the need for additional post-processing operations such as hot isostatic presssing (HIP) to remove defects. Furthermore, the presence of defects leads to lower fatigue strength because defects assist crack propagation.

The chosen range of parameters is highlighted in orange in Figure 3. The middle of this processing window has power of 859W, scanning speed of 1000mm/s and hatch distance of 175µm. These parameters were selected for contour trials.

Laserpower P_L [W]	Hatch distance Δy_S [µm]											
	150			175			200			225		
644	99,99%	99,97%	99,93%	99,99%	99,94%	99,78%	99,90%	99,71%	99,39%	99,41%	99,04%	98,69%
859	99,99%	99,99%	99,98%	99,99%	99,99%	99,98%	99,98%	99,97%	99,92%	99,95%	99,73%	99,62%
	800	1000	1200	800	1000	1200	800	1000	1200	800	1000	1200
	Scanning Speed v_{SCAN} [mm/s]											

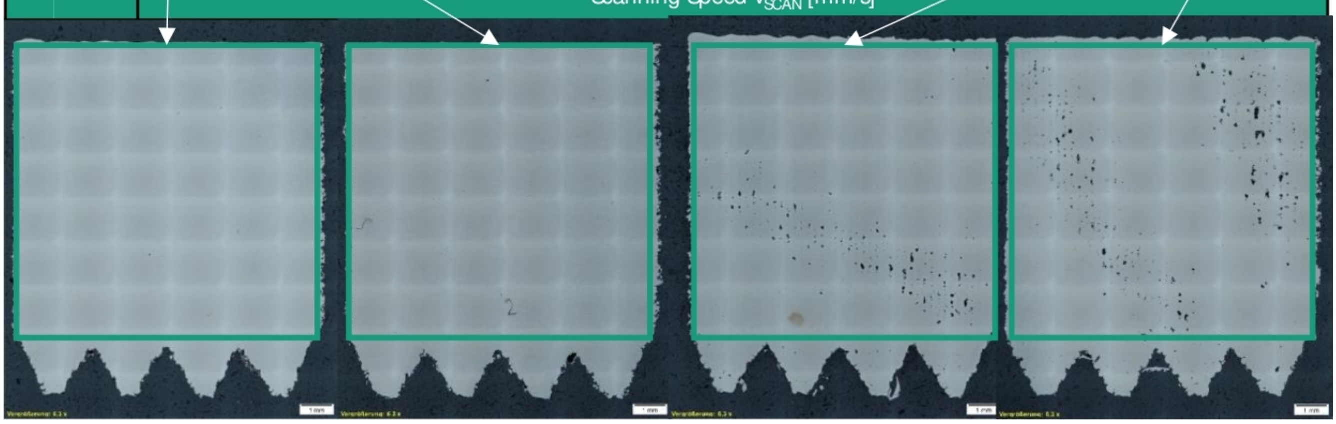

Figure 3: The range of laser parameters (power and hatch distance) found to achieve good density and low defects. Each result is the median from up to six specimens. The chosen parameter range is highlighted in orange.

	Hatch Parameters			Contour Parameters						Roughness
BC [µm]	P_L [W]	v_{SCAN} [mm/s]	ΔyS [µm]	P_L [W]	v_{SCAN} [mm/s]	Contour Vectors	$\Delta y_{S,K}$ [µm]	D_S [µm]	Scanning Order	S_A [µm]
100	644	800	150	644	1200	1	-	60	C→H	22
	644	1200	150	644	1200	1	-	60	C→H	23
	859	800	175	644	1200	1	-	60	C→H	32
	644	1200	175	644	1200	1	-	60	C→H	23
	859	1200	175	644	1200	1	-	60	C→H	28
	859	1200	200	644	1200	1	-	60	C→H	26
250	859	1200	175	644	1200	1	-	30	C→H	40
	859	1200	175	644	1200	2	60	30	C→H	43
	859	1200	175	644	1200	1	-	60	C→H	32
	859	1200	175	644	1200	2	60	60	C→H	48
	859	1200	175	644	1200	1	-	60	H→C	38
50	859	1000	175	644	1200	1	-	60	H→C	35
	859	1200	175	538	1200	1	-	60	H→C	36
	859	1200	175	644	1200	1	-	60	H→C	38
	859	1000	175	644	1200	1	-	60	C→H	30
	859	1200	175	538	1200	1	-	60	C→H	31
	859	1200	175	644	1200	1	-	60	C→H	33

Figure 4: Summary of parameters investigated for contour optimisation.

4.2. Contour trials

Contour parameters affect the quality of the outside surface of the part, in terms of its geometric accuracy, surface finish and defects/pores. Relevant parameters are the laser power and scanning speed (as for bulk density), but also the distance between the contouring vector and hatch boundary, the number of contours (and contour spacing if using multiple contours, Δy_{sk}) , beam compensation, layer thickness (D_S) and whether the contour operation is done before or after the hatch operation.

Contour process development was conducted to minimize the surface roughness without lowering the density underneath the surface of the built component. Table 4 shows the contour parameter sets that were investigated: the hatch laser power, scanning speed, contour laser power, contour/hatch order and the number of contours (and spacing if multiple contours). Contour laser power was first varied from 538 W to 644 W at constant scanning speed of 1200 mm/s. Beam compensation was varied between 50 µm and 250 µm, which was then downselected to 50µm because this showed the optimal dimensional accuracy of the cube samples. With optimal geometric accuracy and low surface roughness, the selected parameter set for contouring was chosen to be a single contour, with scanning order contour-then-hatch, laser power 644W, scanning speed of 1200mm/s and beam compensation of 50µm.

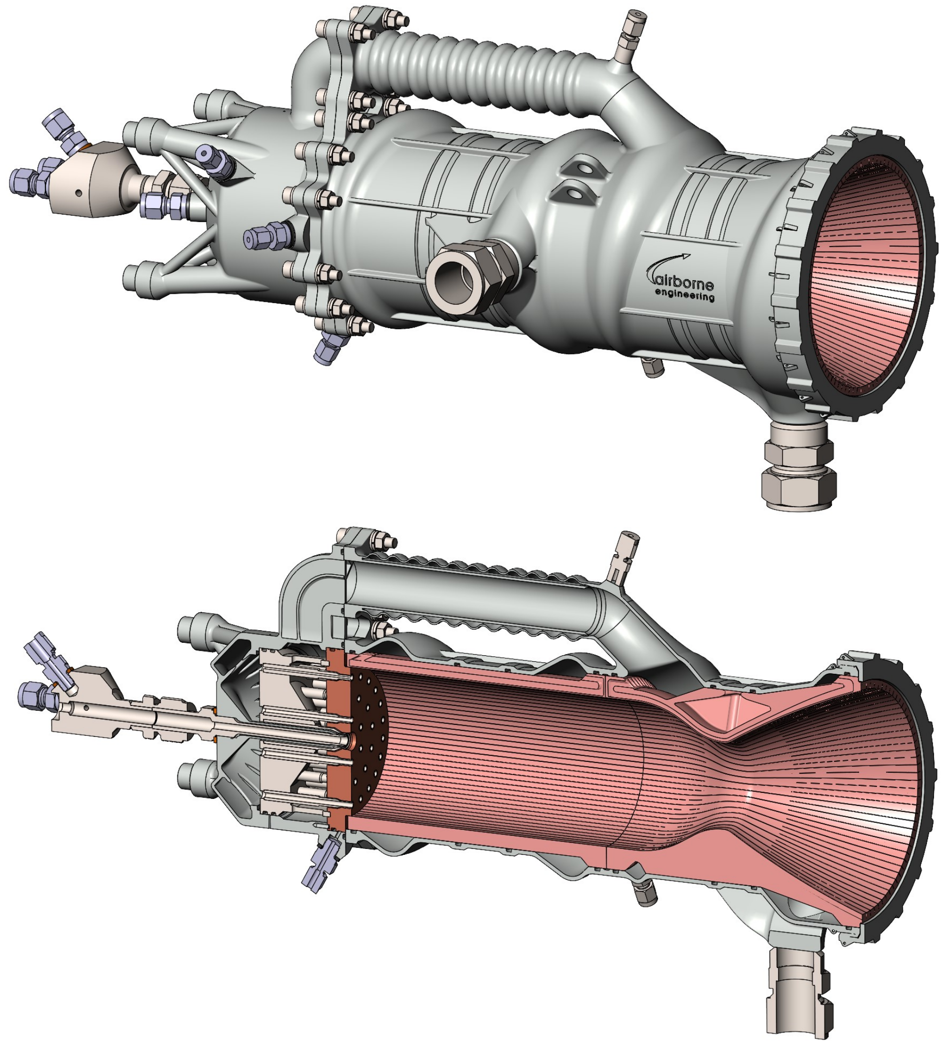

Figure 5: Combustion chamber demonstrator design, which uses two GRCop-42 slip liners that are separately cooled by LOX (chamber) and LCH4 (nozzle). The structural jacket and injector head are printed from IN718, with conventionally machined and brazed injector components.

5. COMBUSTION CHAMBER DEMONSTRATOR

A combustion chamber demonstrator was designed to guide the geometry requirements for the laser process development, and to test printed GRCop-42 samples in a representative environment. The demonstrator is for research purposes, where simplicity and the ability to change components is more important than being flightweight. The main design constraint was the small build volume of the research machine used for GRCop-42, which limited part size to 150mm diameter and less than 170mm in build height. Copper liners are typically used in higher thrust engines, where the combustion chamber needs to be longer than 170mm, and therefore a two-part liner was required.

Figure 5 shows the 20kN scale demonstrator, designed for a nominal chamber pressure of 60bar. It has a two-part GRCop-42 liner, dual-cooled by LOX in the chamber section and LCH4 in the nozzle section, with a structural jacket and injector head additively manufactured from Inconel 718. The copper slip-liners are not bonded to the structural jacket in order to allow them to be removed, examined and replaced, and in order to provide depowdering access to individual channels. Slip-liners have been used successfully by NASA with their GRCop-lined research chambers [15] and have several additional benefits. First, that no bonding trials are required; and second, that thermal contraction/expansion is allowed in the axial direction between the liner and jacket. For bonded liners/jackets, large stresses can arise due to differential thermal expansion during start-up, shutdown, and steady state operation. However, a slip-liner configuration does require the liner to be thick enough to avoid buckling at start-up due to the radially inward force from the coolant pressure. The liners are restrained by a threaded ring at the nozzle exit, which is secured with lockwire. A saddle is printed around the nozzle area in order to maintain the part outer diameter and allow o-ring seals between the LCH4 inlet and outlet manifolds. This saddle has radial ribs for buckling resistance, and lattice infill in between ribs.

The demonstrator has 88 coolant channels with bifurcations in the nozzle contraction and expansion regions. To encourage an even massflow distribution across the coolant channels, the inlet and outlet manifolds have variable area, and the entries to the manifolds are split and swept such that the fluid direction has a circumferential component to reduce the pressure spike opposite the inlet. The gasified methane returns to the injector head through a lined pipe with external printed bellows. Due to limitations on print angle and wall thickness, a printed bellows is not as flexible as a traditional electroformed bellows but should reduce the thermal stress sufficiently.

The injector design is based on the published results from DLR's LUMEN [16, 17] and BKD engines [18], due to the similarity in operating conditions. The injector uses a copper faceplate with shear coaxial elements and a central port for ignition. AEL's standard oxidant-rich hydrogen/oxygen gas torch igniter is used, with additional hydrogen augmentation at the injector face. This flow of hot ignition gas is located concentrically within an enlarged LOX/LCH4 coaxial injector, in order to provide increased ignition enthalpy during engine startup. Instrumentation tappings are provided for chamber pressure, and pressures and temperatures within the jacket and injector manifolds.

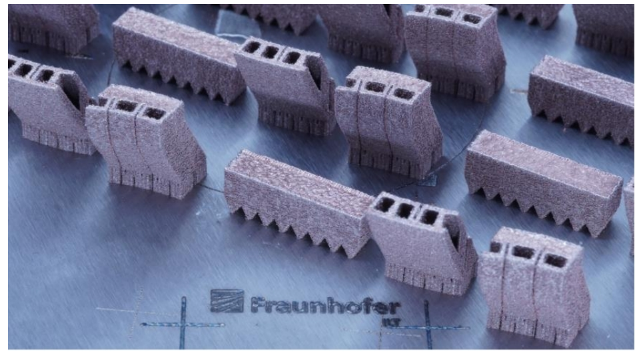

Figure 7: Trial build of key coolant channel geometries.

5.1. Geometry samples

Small samples were printed for key areas to examine the as-printed geometry and ensure that the beam compensation parameter was correct. Figures 6 and 7 show trial builds for the coolant channels at the throat and the channel bifurcation in the nozzle convergence, which is where the coolant channels have minimum width. The channel dimensions are reproduced well, but with significant channel roughness.

5.2. Expansion slots for firewall compliance

During hot-firing a LRE firewall undergoes cyclic loading due to thermal and pressure stress during start-up and shutdown, and thermal stresses during operation. For a cryogenic engine, during start-up the copper firewall chills down faster than the structural jacket causing a tensile stress in the firewall alongside the pressure stress. After ignition the firewall heats rapidly, whereas the jacket does not, leading

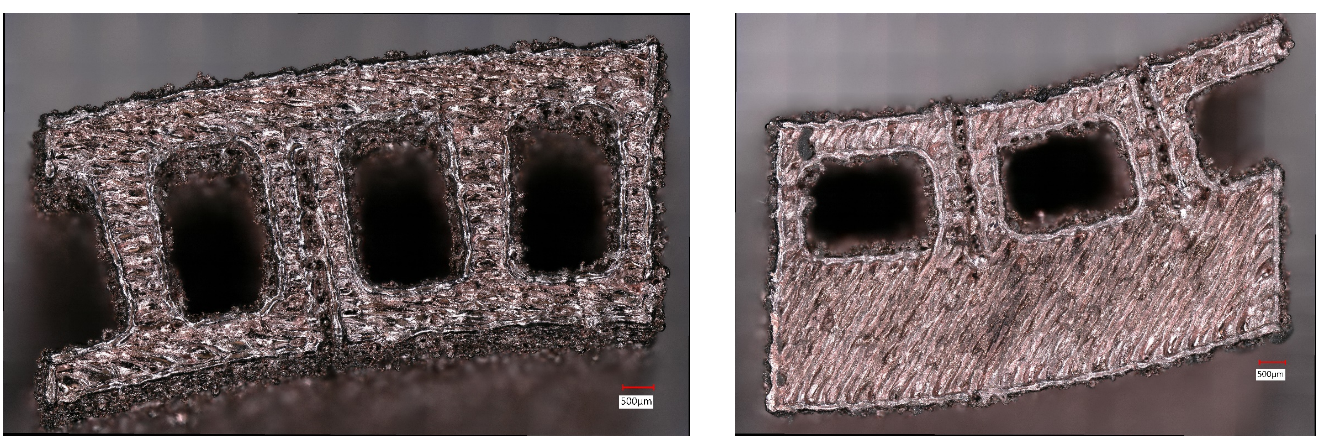

(a) Bifurcation area (nozzle convergence)

(b) Throat area

Figure 6: Trial build of coolant channels at the bifurcation (nozzle convergence) and throat areas.

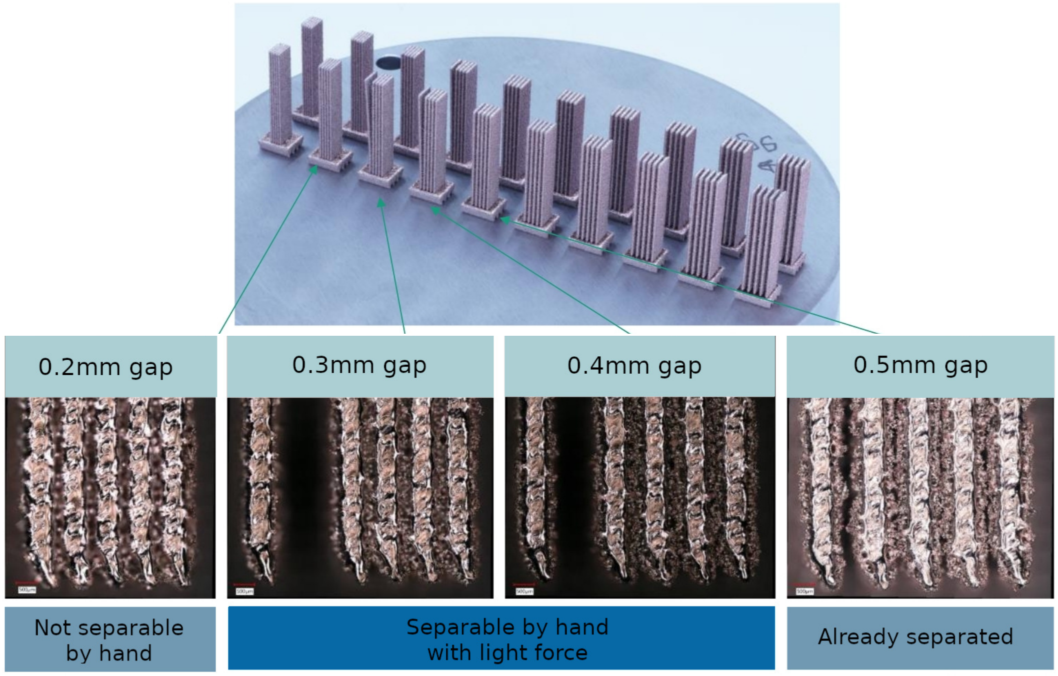

Figure 8: Trial build of narrow gaps between vertical walls. Partially sintered material is visible in the narrow gaps.

to a compressive stress in the firewall [1]. At shutdown the firewall cools rapidly again, causing a tensile stress in the firewall. The cyclic strain can have compressive and tensile strains of roughly 1-2%; the LE-9 engine has simulated strains of -2.2% to +1.0% [1]. Combustion chambers firewalls therefore typically fail from a combination of LCF and cyclic plastic strain accumulation (ratchetting) for each start-up and shutdown, and high temperature creep from steady-state operation, resulting in a 'dog-house' failure mode.

The strain range during cycling has a very strong effect on lifetime; halving the strain range for wrought GRCop-42 results in almost an order of magnitude higher lifetime [22]. One method of reducing the cyclic strain range is to allow gaps in between coolant channels [23, 24, 25]. Ref [23] presents experimental lifetime results for a combustion chamber with individually machined OFHC copper channels that were bonded at their external surface using electroforming; these channels had no gaps between them but each channels was unconnected to its neighbour. This reduced the total strain cycling in several ways: first, no tensile stress could transfer between channels during pre/post cooling, and second, the radial channel walls can bend and twist in order to allow the firewall to shrink or bow out, which reduces the maximum strains experienced. The experimental results of Ref. [23] showed that the chamber lifetime increased by a factor of 3, and changed the failure mode from LCF dog-house failure to tensile failure of the OFHC copper due to grain coarsening at high temperature. GRCop-42 will be more resistant to grain coarsening than OFHC copper and therefore should have an even higher increase in lifetime.

Additive manufacture allows combustion chambers to be printed with expansion gaps with no additional process overhead. The demonstrator combustion chamber therefore has a novel geometry which includes printed expansion gaps in between the coolant channels. The walls in between the channels are vertical, which makes printing a narrow gap easier. Figures 6 and 7 show examples of as-printed expansion gaps, aiming for a 0.2mm gap. Additive manufacture leads to large surface roughness, however, so the as-printed expansion gap is not simply an air gap between two smooth walls, but has two rough walls, and as gap-size decreases there will be some trapped and partially-sintered powder. For very small gap sizes there may be bridging between the surface roughness of the two walls (Figure 8).

For a 3mm wide coolant channel an ideal expansion gap would have an air-gap of roughly 30µm, in order to allow 1% compressive movement with no stress, and have no connection to its neighbouring channel, so that there is no tensile stress at all between channels. The rough partially sintered material between as-printed coolant channels will not behave this way, however, because it will plastically deform under compression, but with a much lower modulus than for solid material. Rough surfaces will discourage hot-gas flow within the gap, which is beneficial.

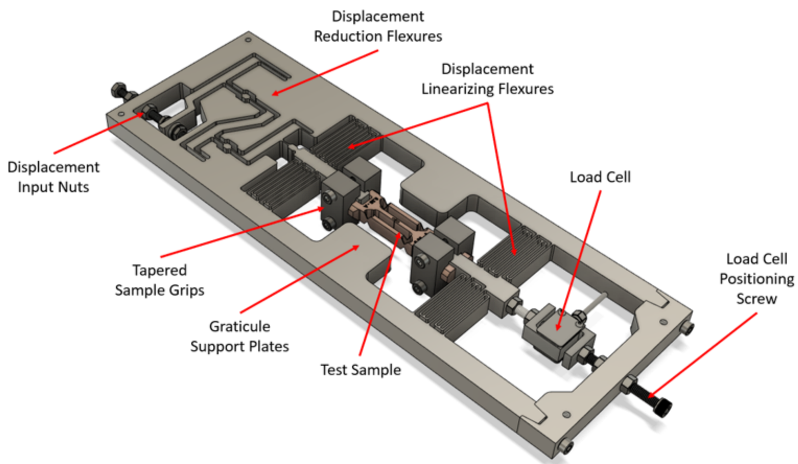

(a) Tensile test rig

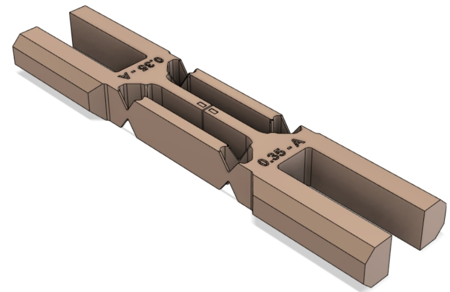

(b) Expansion gap test sample

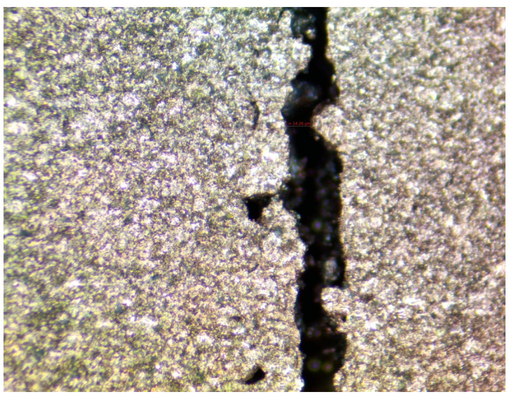

(c) 0.35mm sample (unloaded)

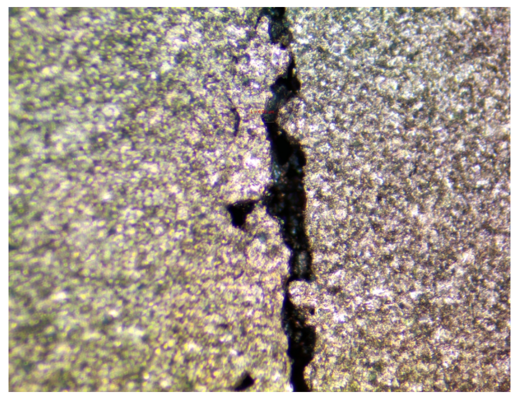

(d) 0.35mm sample (500N compression)

Figure 9: Tensile test rig for applying small displacements to the expansion gap test samples (a). The displacement was measured optically using a microscope, with measurements taken when unloaded (c) and loads up to 500N (d). Example test data is presented for samples printed with 0.50mm, 0.35mm and 0.15mm expansion gaps.

5.2.1. Tensile testing

Experiments were required in order to characterise the performance of as-printed expansion gaps, in terms of their response to compression and tension. Standard laboratory tensile testing equipment would have had difficulty in measuring subtle changes in gap width at low forces, so a custom tensile test rig was designed and built. Figure 9a shows this test rig. A set of flexures was waterjet cut from a sheet of stainless steel, to allow a 35:1 reduction in axial displacement from turning a driving screw to moving the expansion gap. Two sets of linearising flexures keep this displacement axial whilst adding minimal linear force themselves. A printed sample with an expansion gap is restrained by two tapered grips. A load cell is used to measure the linear force, whilst the gap width is measured optically using a microscope.

The test procedure was as follows. A new sample was clamped into the rig at zero axial load. A calibration graticule was used to set the length scale for subsequent microscope images, and a datum image of the gap was taken (Figure 9c) and a datum gap feature identified. Each sample has removable side features to prevent distortion of the gap during travel, which were then cut. The samples were then slowly loaded in compression in steps up to 500N, which was the maximum limit of the load cell. At each step the load was recorded, and the change in gap width measured by measuring the distance between two obvious features on the image. Once the sample had been loaded to 500N (Figure 9d) compression, it was then unloaded and taken into tension, before being loaded back to 500N compression again to determine whether material deformation had been elastic or plastic.

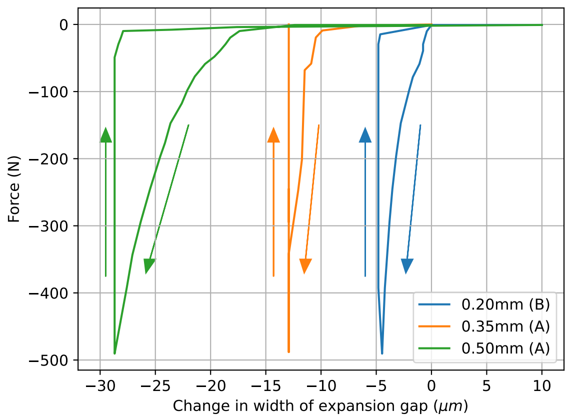

Figure 10: Expansion gap tensile testing results, for three different gap sizes. Arrows denote the direction of the loading with respect to time. No tensile response was seen.

Sixteen samples were tested with a range of printed gap sizes (0.15mm, 0.20mm, 0.25mm, 0.35mm and 0.50mm). Figure 10 shows example data from three samples. For the 0.35mm and 0.50mm samples there is an actual air-gap, with air-gap sizes of roughly 10 µm and 17µm respectively before any compressive force is seen. Beyond compression of the air gap there is then plastic deformation of partially sintered material until the maximum load of 500N, which corresponds to an average compressive stress of 17MPa over the sample. This average stress is much lower than the elastic limit, because the plastic deformation is concentrated locally on high-points of the rough surface. All load is then removed without any movement, showing that the deformation was plastic and not elastic. After compression, no sample could sustain any tensile force; the two halves of the sample were separate pieces.

These initial tensile tests demonstrated that by printing expansion gaps it is (a) possible to entirely remove tensile stress between channels, and (b) allow stress-free circumferential expansion of the firewall of roughly 10 µm per channel, which becomes roughly 15 µm after one compressive cycle. This will significantly reduce the cyclic strain range and therefore significantly increase chamber lifetime, with no additional processes and minimal weight penalty.

5.3. Transpiration cooling

In contrast to film cooling, where a coolant is injected through discrete holes of finite size, idealised transpiration cooling uses an infinite number of infinitely small holes to uniformly spread a cooling layer of propellant over the firewall surface. Additive manufacture is not good at printing tiny holes with reproducable flow areas, however, particularly as the hole size nears the powder diameter. Printing porous material with PBF is possible for horizontal surfaces by changing the hatching distance, but is more difficult for vertical walls (such as the firewall) and it also adds weak points to the firewall which is undesirable.

The novel printed expansion gap geometry also has an additional potential benefit, in that it can be used to allow transpiration cooling. As shown in Figure 8, printed expansion gaps can be very narrow (~15µm) and have very rough walls. A hole can be used to feed propellant from the coolant channels into the gap, and this hole can be large enough to be easily reproduced and depowdered, because the flowrate is limited by the gap and not the hole.

Figure 11 shows a flow test sample that was printed to demonstrate transpiration cooling through expansion slots. The sample has 11 cooling channels with water fed from a manifold at one end. A pressure transducer measures pressure through a manifold at the other end. The sample has 60 x 0.5mm diameter teardrop shaped holes placed on a staggered grid over an area of roughly 59x36mm, which connect the coolant channels to the bottom of the expansion slots.

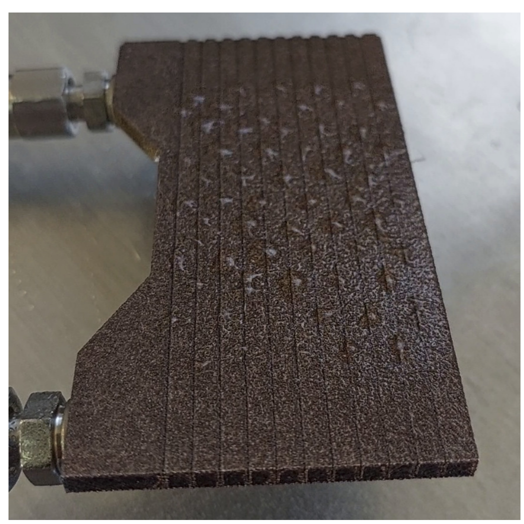

Figure 11: Transpiration cooling sample. A staggered grid of 60 x 0.5mm diameter holes flows into a dummy firewall with 0.2mm expansion gaps between 11 channels.

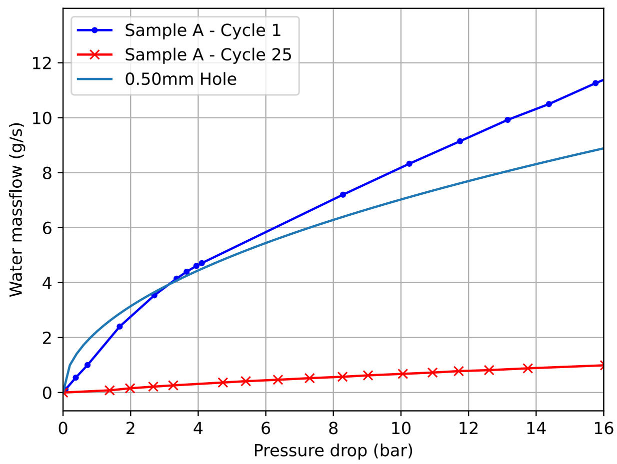

Figure 12: The total massflow through 60 transpiration cooling holes is similar to that from a single machined 0.5mm hole. The flow rate of the transpiration cooling sample was noted to decrease over number of cycles, however.

Flow tests with air and water were undertaken at a variety of feed pressures. Figure 12 shows example data from one sample. The flow through all holes was qualitatively uniform, but no massflow measurements were taken for individual holes. The water exiting the gaps had almost no velocity. On the first pressure cycle the total flow rate was roughly equivalent to the theoretical value for a single 0.5mm diameter machined hole; in other words, the transpiration cooling geometry was able to spread the flowrate from a single hole uniformly across sixty. The average flow rate across the sample was roughly 0.5 g/s.cm^2 at 16bar. A second identical sample reproduced these results closely. Subsequent pressure cycles showed that the transpiration flowrate decreased with cycle number. This could have been due to fine residue in the water flow system blocking the partially sintered material, or due to plastic deformation closing up the partially sintered material. Cyclic test data suggested the plastic deformation is the most plausible explanation, but this can be verified with further testing.

These transpiration cooling flow tests demonstrated that it is possible to use additively manufactured expansion gaps to both reduce firewall stresses and to distribute a small amount of coolant film across a large surface area. The transpiration cooling will further reduce firewall stresses. Furthermore, with additive manufacture it is easy to tailor the firewall cooling by placing these transpiration features only where they are most required, such as in the nozzle contraction and throat area, or in discrete bands in the cylindrical part of the chamber.

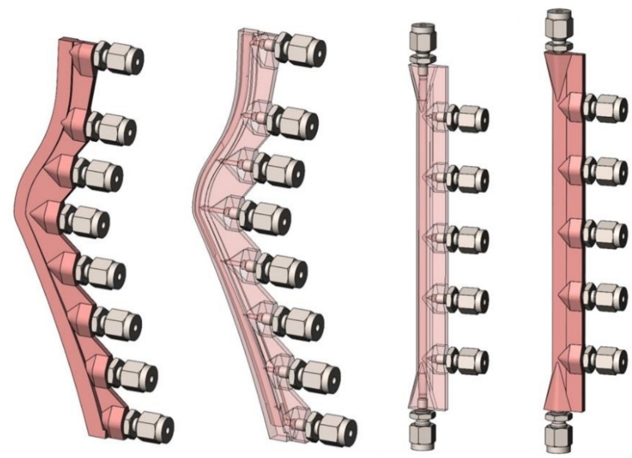

Figure 13: Single-channel test pieces from both the chamber and nozzle liners were printed for flow testing, to measure the as-printed surface roughness.

5.4. Flow testing samples

The surface roughness of PBF parts is a strong function of build angle, and therefore surface roughness results from vertical samples cannot be extrapolated to nozzle geometries, where the convergence and divergence sections have a significant deviation from vertical. Figure 13 shows single-channel test pieces that were printed in order to ascertain the effect of surface roughness on coolant pressure drop. These were flow tested with water, using a Coriolis meter to measure flowrate and pressure transducers to measure pressure drop along the channel. The pressure loss was significantly higher in the nozzle section than had been assumed for the original engine cooling calculations, and the coolant channel height in the nozzle region had to be increased. Chemical techniques for reducing surface roughness in printed copper channels have been shown to be effective [21] but are beyond the scope of this programme. Light mechanical polishing of the firewall will be undertaken in order to reduce hot-gas heat flux [21].

5.5. Thermal analysis

The coolant channel geometry was designed using AEL's in-house heat transfer code, which couples an empirical hot-gas heat transfer model with a 3D finite-element conduction solver and a 1D coolant model. This uses empirical heat transfer correlations for the methane [19] and oxygen coolants [20], with modification factors to allow for the increased roughness of the as-printed walls [26].

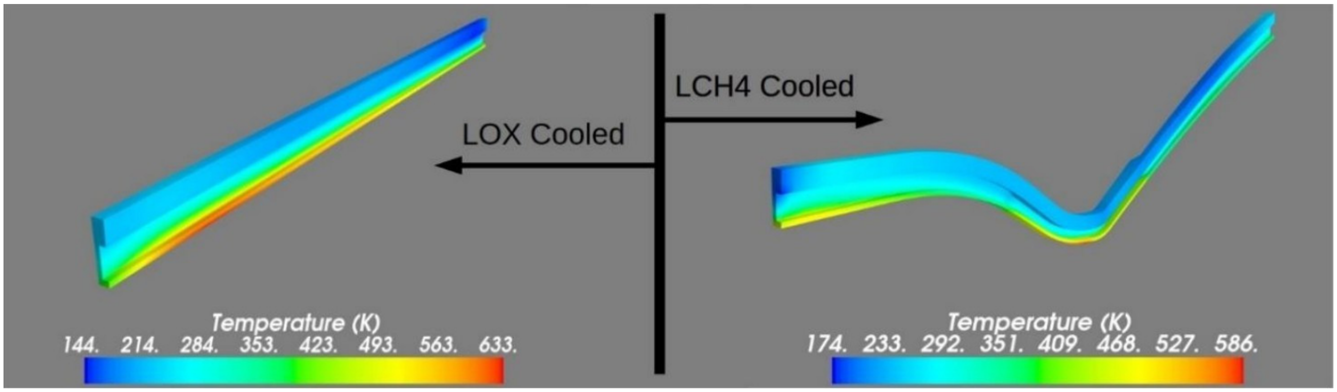

Figure 14: Example thermal analysis results for the GRCop-42 liner at one operation condition.

Figure 14 shows example metal temperature results from the heat transfer analysis. The firewall temperatures peak locally at the throat, where the heat flux is highest, and also peaks towards the injector face where the heat flux rises and the oxygen has dropped in density and the coolant side heat transfer therefore deteriorates.

6. STATUS AND FURTHER WORK

Full size liners have been printed in order to de-risk manufacture of the liner geometry and test post-machining operations. A second set of liners will be printed to incorporate the taller channels at the throat that were required post flow testing. The Inconel jacket and injector head are currently entering manufacture. Once complete, the demonstrator engine will be hot-fired with LOX/LCH4 at AEL's J1 facility at Westcott, UK, in order to verify the performance of the green laser GRCop-42 material under representative conditions.

Further testing will also be undertaken for the novel transpiration cooling geometry, with simple geometry modifications which should improve the repeatability of results, reduce the effect of plastic deformation and number of cycles, and allow even more uniform distribution of flow.

7. CONCLUSION

Green lasers have higher power absorption for copper alloys than traditional red laser systems, and therefore should be better for producing high density, low-defect PBF parts. Green laser processes were optimised using small coupons and parameter sweeps of laser power, hatch distance, scanning speed and beam compensation. Excellent bulk densities of up to 99.99% were obtained, and the resulting mechanical properties were measured. Such high bulk density means that downstream hot-isostatic pressing (HIP) processes are no longer required to close up porosity.

AEL designed a 20kN scale demonstrator combustion chamber, to be dual-cooled by LOX/LCH4. The design features an additively manufactured IN718 jacket and two-part additively manufactured GRCop-42 slip liner. Small samples and full liner geometries have been built.

A novel expansion slot geometry is printed into the firewall to allow thermal expansion and contraction during engine transients and steady state operation. This compliance reduces stresses in the firewall and should therefore increase chamber lifetime significantly. Bench tests of the expansion slots were undertaken to measured gap compliance as a function of print geometry. These expansion slots were also shown to potentially be useful for controlled distribution of transpiration coolant, which can be used to reduce firewall stresses further during engine operation.

Figure 15: Combustion chamber liners as-printed.

8. ACKNOWLEDGEMENTS

The CufAM programme is an ESA GSTP programme with funding contributions from the UKSA and DLR, under ESA technical oversight of Martina Meisnar. The authors also wish to thank project collaborators Nick Cruchley, Angharad Ameline, Marvin Kippels and Tim Lantzsch for their contributions.

REFERENCES

[1] Deguchi, M. (2016). Damage propagation mechanism in low-cycle creep fatigue of Cu-Cr-Zr alloy, *International Journal of Fatigue*.

[2] Becker, D. (2014). Selektives Laserschmelzen von Kupfer and Kupferlegierungen, Apprimus Wissenschaftsverlag, Aachen.

[3] Horn, M. et al. (2022). Powder Bed Fusion of highly filigree copper features using a green laser, *12th CIRP Conference on Photonic Technologies*.

[4] Jadhav, S. et al. (2019). Mechanical and electrical properties of selective laser-melted parts produced from surface-oxidized copper powder, *Material design and processing communications*.

[5] Jadhav, S. et al. (2019). Selective laser melting of copper and copper alloys: issues and remedies, *9th Internation Conference - Additive Manufacturing Society of India*.

[6] Minneci, R. (2020). Copper-based alloys for structural high-heat-flux applications: a review of development, properties, and performance of Cu-rich Cu-Cr-Nb alloys, *International Materials Reviews*.

[7] Gradl, P. et al (2018). Additive Manufacturing of Liquid Rocket Engine Combustion Devices: A Summary of Process Developments and Hot-Fire Testing Results, *54th AIAA/SAE/ASEE Joint Propulsion Conference*.

[8] Moriya, S. et al. (2018). Feasilibility study on additive manufacturing of liquid rocket combustion chamber, *Trans JSASS Aerospace Tech. Japan*, 16 (3).

[9] Waugh, I. et al. (2021). Additive manufacture of rocket engine combustion chambers from CuCrZr (C- 18150) using the DMLS process, *Space Propulsion 2020+1*.

[10] Gradl, P. et al. (2021), Advancing GRCop-based Bimetallic Additive Manufacturing to Optimize Component Design and Applications for Liquid Rocket Engines, *AIAA Propulsion and Energy Forum*.

[11] Gradl, P. (2019). Progress in additively manufactured copper-alloy GRCop-84, GRCop-42, and bimetallic combustion chambers for liquid rocket engines, *Proceedings of the 70th International Astronautical Congress*.

[12] Launcher Space (2018). https://www.instagram.com/p/Bq0bVCMAetf

[13] Launcher Space (2020). https://launcherspace.com/engine-2

[14] Ellis, D. and Michal, G. (1996). Mechanical and thermal properties of two Cu-Cr-Nb alloys and NARloy-Z, *NASA CR-198529*.

[15] Gradl, P. et al. (2017). Development and hot-fire testing of additively manufactured copper combustion chambers for liquid rocket engine applications, *53rd AIAA/SAE/ASEE Joint Propulsion Conference*.

[16] Hardi, J. et al. (2020), Lumen thrust chamber - Injector performance and stability, *Space Propulsion 2020+1*

[17] Börner, M. et al. (2020), Lumen thrust chamber - Flame anchoring for shear coaxial injectors, *Space Propulsion 2020+1*

[18] Armbruster, W. et al. (2022). Impact of shear-coaxial injector hydrodynamics on high-frequency combustion instabilities in a representative cryogenic rocket engine, *International Journal of Spray and Combustion Dynamics*.

[19] Giovanetti, A. et al. (1984). Deposit formation and heat transfer in hydrocarbon rocket fuels, *AIAA 22nd Aerospace Sciences Meeting*.

[20] Spencer, R. and Rousar, D. (1977). Supercritical oxygen heat transfer, *NASA CR-135339*.

[21] Teasley, T. et al. (2021). Extreme environment hot fire durability of post processed additively manufactured GRCop-alloy combustion chambers, *AIAA Propulsion and Energy Forum*.

[22] Gradl, P. et al. (2019). GRCop-42 Development and hot-fire testing using additive manufacturing powder bed fusion for channel-cooled combustion chmambers, *55th AIAA/SAE/ASEE Joint Propulsion Conference*

[23] Pavli, A. et al. (1992). Hot fire fatigue testing results for the compliant combustion chamber, *NASA TP-3223*.

[24] Jankovsky, R. et al. (1994). Structurally compliant rocket engine combustion chamber - Experimental and analytical validation, *NASA TP 3431*.

[25] Quentmeyer, R., Rocket combustion chamber life-enhancing design concepts, *NASA CR 185257*.

[26] Norries, R. (1971). Augmentation of convection heat and mass transfer, *ASME*.